Science Advances
AAAS

advances.sciencemag.org/cgi/content/full/5/7/eaaw7243/DC1

Supplementary Materials for

Cell sensing and decision-making in confinement: The role of TRPM7 in a tug of war between hydraulic pressure and cross-sectional area

Runchen Zhao, Alexandros Afthinos, Tian Zhu, Panagiotis Mistriotis, Yizeng Li, Selma A. Serra, Yuqi Zhang, Christopher L. Yankaskas, Shuyu He, Miguel A. Valverde, Sean X. Sun, Konstantinos Konstantopoulos*

*Corresponding author. Email: konstant@jhu.edu

Published 24 July 2019, *Sci. Adv.* **5**, eaaw7243 (2019)
DOI: 10.1126/sciadv.aaw7243

This PDF file includes:

Fig. S1

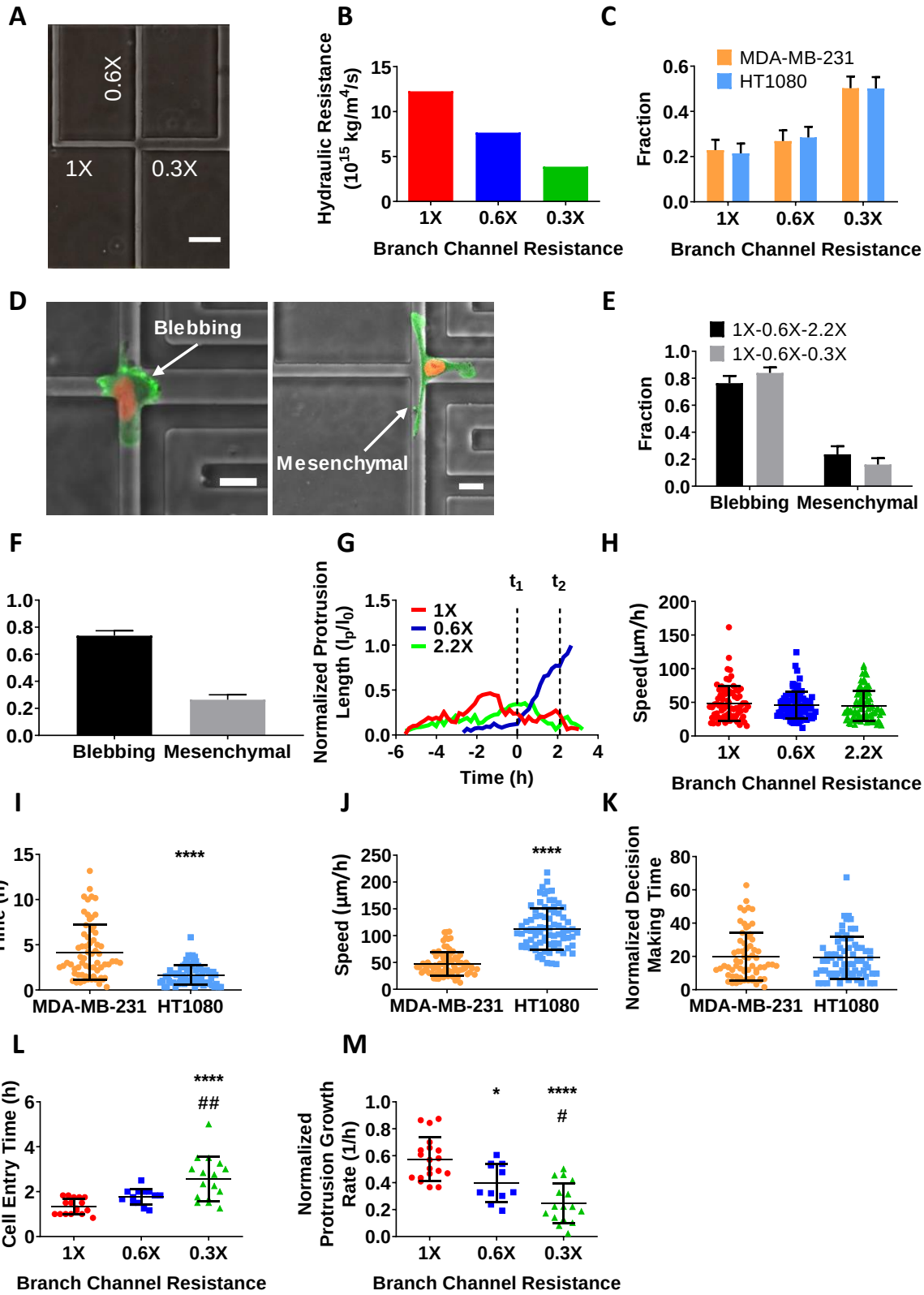
A
0.6X
1X
0.3X
B
Hydraulic Resistance (10^{15} kg/m^4/s)
Branch Channel Resistance
C
MDA-MB-231
HT1080
Fraction
Branch Channel Resistance
D
Blebbing
Mesenchymal
E
1X-0.6X-2.2X
1X-0.6X-0.3X
Fraction
Blebbing
Mesenchymal
F
Fraction
Blebbing
Mesenchymal
G
Normalized Protrusion Length (l_p/l_0)
t_1
t_2
1X
0.6X
2.2X
Time (h)
H
Speed (μm/h)
Branch Channel Resistance
I
Decision Making Time (h)
****
MDA-MB-231
HT1080
J
Speed (μm/h)
****
MDA-MB-231
HT1080
K
Normalized Decision Making Time
MDA-MB-231
HT1080
L
Cell Entry Time (h)
****
##
Branch Channel Resistance
M
Normalized Protrusion Growth Rate (1/h)
*
****
#
Branch Channel Resistance

Fig. S1. Characterization of cell decision-making at trifurcating Ψ-like branch channels of different hydraulic resistances. (**A**) Phase contrast image of a different Ψ-like trifurcating microfluidic device. The relative hydraulic resistance of each branch channel is indicated. Scale bar: 50 μm. (**B**) Absolute values of the hydraulic resistance of each branch channel in fig. S1A. (**C**) Distribution pattern of MDA-MB-231 and HT1080 cells in branch channels of different hydraulic resistances (n>300 from 3 independent experiments for each cell line). Data represent the mean with 95% confidence interval. (**D**) Representative images of LifeAct-GFP H2B-mCherry MDA-MB-231 cells at the intersection depicting blebbing (left) and mesenchymal (right) phenotypes during decision-making. Scale bar: 20 μm. The contrast of the fluorescent signals has been increased in all images uniformly for visualization purposes. (**E**) Fraction of MDA-MB-231 cells displaying blebbing vs. mesenchymal phenotypes in the two different Ψ-like trifurcating microfluidic devices (1X-0.6X-2.2X refers to Fig. 1A and 1X-0.6X-0.3X refers to fig. S1A) (n>200 cells from ≥3 independent experiments for each design). Data represent the mean with 95% confidence interval. (**F**) Fraction of HT 1080 cells exhibiting blebbing vs. mesenchymal phenotypes in the feeder microchannel (n>90 cells from 3 independent experiments). Data represent mean±SD. (**G**) Representative normalized protrusion lengths (l_p / l_0) within the left, straight and right branch channels as a function of time for a cell initially sampling the microenvironment before ultimately choosing the straight branch channel. At t_1 the decision was made and a dominant protrusion (blue line) appears, whereas at t_2 the nucleus fully entered the branch channel at the trifurcation. (**H**) Migration speeds of MDA-MB-231 cells inside the feeder channel prior to reaching the intersection and ultimately committing to enter one of the three branch channels of different hydraulic resistances (n>70 cells from 3 independent experiments). Data represent the mean±SD. (**I**) Decision-making time of MDA-MB-231 and HT1080 cells (n>60 cells from 3 independent experiments). Data represent the mean±SD; Mann-Whitney U test was performed; ****p<0.0001 relative to MDA-MB-231 cells. (**J**) Migration speeds of MDA-MB-231 and HT1080 cells in the feeder channel prior to reaching the intersection (n>80 cells from 3 independent experiments). Data represent the mean±SD; Mann-Whitney U test was performed; ****p<0.0001 relative to MDA-MB-231 cells. (**K**) Normalized decision-making times of MDA-MB-231 and HT1080 cells (n>60 cells from 3 independent experiments) derived by multiplying decision-making time with the migration speed of cells in the feeder channel and dividing by the typical feeder channel dimension of 10 μm. Data represent the mean±SD. (**L**) Cell entry times, t_2-t_1, in branch channels of different hydraulic resistances for the trifurcating microfluidic device shown in fig. S1A (n>10 for each branch channel from >3 independent experiments). Data represent the mean±SD; one-way ANOVA with post-hoc Tukey was performed, ****p<0.0001 relative to cells choosing the left branch; ##p<0.01 relative to cell choosing the straight branch. (**M**) Normalized leading protrusion growth rate for cells entering branch channels of different hydraulic resistances for the trifurcating microfluidic device shown in fig. S1A. Data represent the mean±SD; one-way ANOVA with post-hoc Tukey was performed, *p<0.05, ****p<0.0001 relative to cells choosing the left branch; #p<0.05 relative to cells choosing the straight branch.

Fig. S2

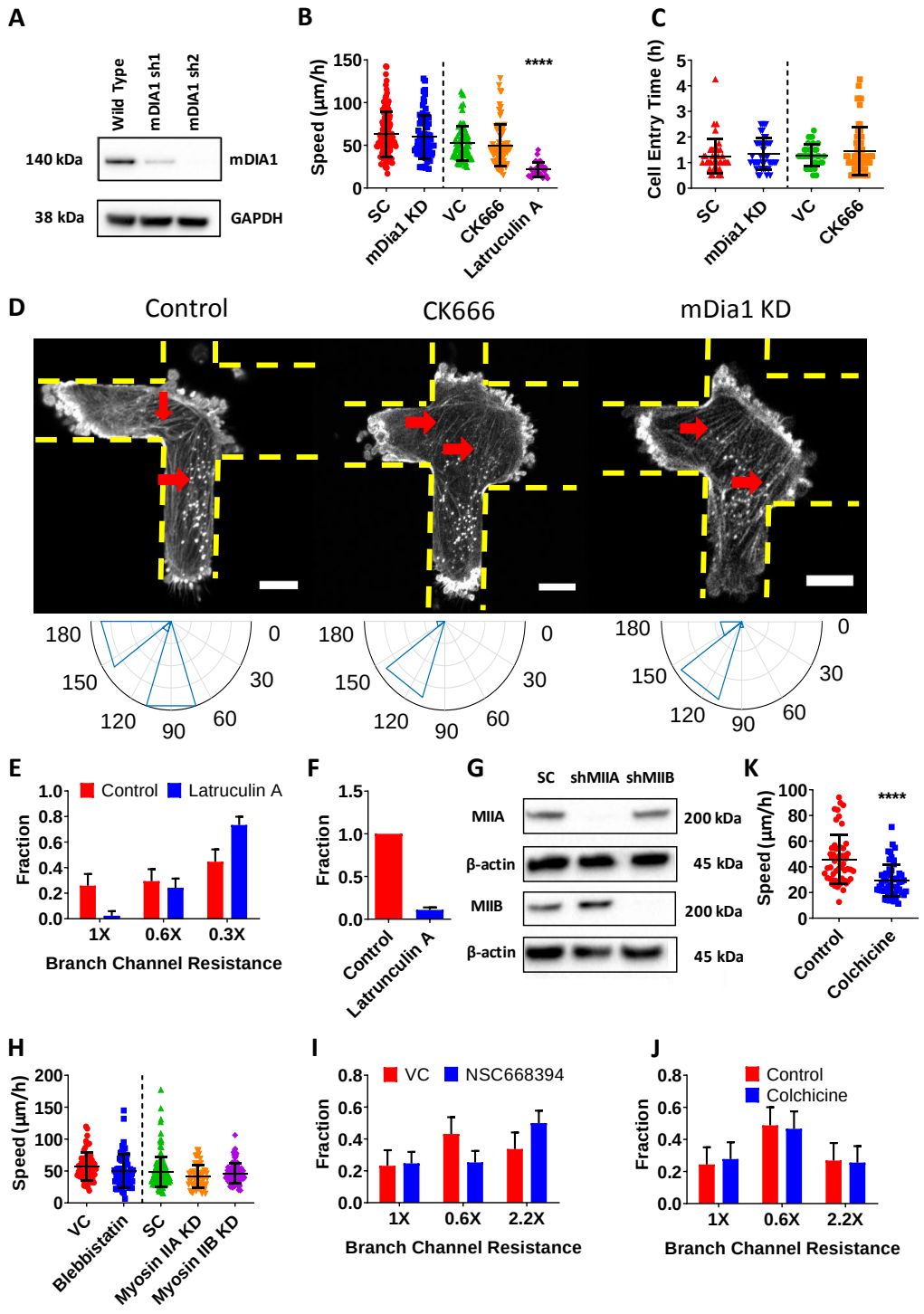

Fig. S2. Effects of different cytoskeletal constituents on cell decision-making in response to hydraulic resistance. (**A**) Representative western blot illustrating the knockdown efficiency of mDia1 in MDA-MB-231 cells using two different shRNA sequences. (**B**) Migration speeds of MDA-MB-231 cells in the feeder channel prior to reaching the intersection in response to different pharmacological (CK666, Latrunculin A) or molecular (mDia1-KD) interventions (n>30 cells from 3 independent experiments). Data represent the mean±SD. Kruskal-Wallis with

post-hoc Dunn was performed; ****p<0.0001 relative to vehicle control. (**C**) Cell entry times of control, CK66-treated or mDia-KD MDA-MB-231 cells (n>30 cells from 3 independent experiments). Data represent the mean±SD. (**D**) Representative confocal microscopy images depicting the basal layer of untreated control, CK666-treated LifeAct-GFP-labeled and and mDia1-KD LifeAct-Ruby2-labeled MDA-MB-231 cells. Arrows indicate stress fibers. The borders of the microchannels are depicted by the yellow dashed lines. Scale bar: 10 μm. Quantitative analysis of the orientation of actin stress fibers is presented below each corresponding image in polar histogram plots. Images were converted to grayscale and the contrast was adjusted uniformly for visualization purposes. (**E**) Distribution patterns of vehicle-control and Latrunculin A-treated MDA-MB-231 cells in branch channels of different hydraulic resistances for the trifurcating microfluidic device shown in fig. S1A (1X-0.6X-0.3X). Data represent the mean with 95% confidence interval. p<0.001 for the distribution of LatA-treated cells versus controls as indicated by chi-squared test. (**F**) Fraction of vehicle control and Latrunculin A-treated MDA-MB-231 cells which successfully made decisions at the intersection. Data represent the mean±SD. (**G**) Representative Western blot illustrating the knockdown efficiency of shMIIA and shMIIB on MDA-MB-231 cells. (**H**) Migration speeds of MDA-MB-231 cells in the feeder channel in response to different pharmacological (blebbistatin) or molecular interventions (Myosin-IIA or Myosin-IIB knockdown) (n>60 cells from 3 independent experiments). Data represent the mean±SD. (**I**) Distribution pattern of vehicle control and NSC668394-treated MDA-MB-231 in branch channels of different hydraulic resistances (n>30 cells from 3 independent experiments). Data represent the mean with 95% confidence interval. p<0.0001 for the distribution of NSC668394-treated cells versus controls as indicated by chi-squared test. (**J**) Distribution pattern of vehicle control and colchicine-treated MDA-MB-231 cells in branch channels of different hydraulic resistances (n>80 cell from 3 independent experiments). Data represent the mean with 95% confidence interval. (**K**) Migration speeds of vehicle control and colchicine-treated MDA-MB-231 cells in the feeder channel before reaching the intersection (n>50 cells from 3 independent experiments). Data represent the mean±SD. Mann-Whitney U test was performed; ****p<0.0001 relative to vehicle control cells.

Fig. S3

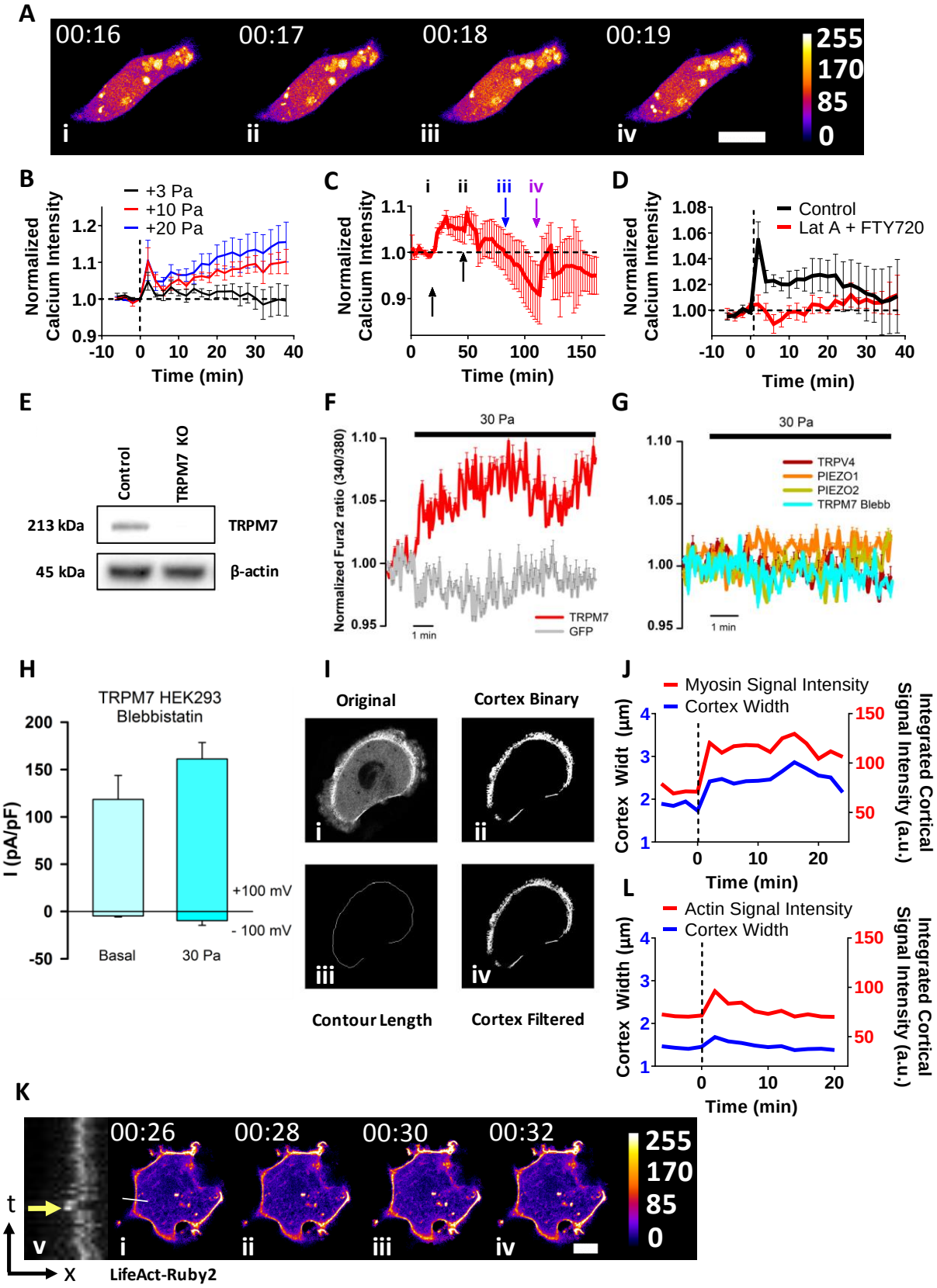
A
00:16
00:17
00:18
00:19
i
ii
iii
iv
255
170
85
0
B
+3 Pa
+10 Pa
+20 Pa
Normalized Calcium Intensity
Time (min)
C
i
ii
iii
iv
Normalized Calcium Intensity
Time (min)
D
Control
Lat A + FTY720
Normalized Calcium Intensity
Time (min)
E
Control
TRPM7 KO
213 kDa
TRPM7
45 kDa
β-actin
F
30 Pa
Normalized Fura2 ratio (340/380)
1 min
TRPM7
GFP
G
30 Pa
TRPV4
PIEZO1
PIEZO2
TRPM7 Blebb
1 min
H
TRPM7 HEK293
Blebbistatin
I (pA/pF)
+100 mV
- 100 mV
Basal
30 Pa
I
Original
Cortex Binary
Contour Length
Cortex Filtered
J
Myosin Signal Intensity
Cortex Width
Cortex Widt (µm)
Integrated Cortical Signal Intensity (a.u.)
Time (min)
L
Actin Signal Intensity
Cortex Width
Cortex Width (µm)
Integrated Cortical Signal Intensity (a.u.)
Time (min)
K
00:26
00:28
00:30
00:32
255
170
85
0
t
X
v
i
ii
iii
iv
LifeAct-Ruby2

Fig. S3. Hydrostatic pressure induces intracellular calcium increase and a thicker cortical actin meshwork. (**A**) Representative image sequence of an MDA-MB-231 cell on 2D showing the Fluo-4 Direct signal intensity before and after the application of a 3 Pa hydrostatic pressure differential. Pressure is increased right after (**ii**). Each pixel's intensity value was assigned a color according to ImageJ's fire heat map for better visualization of calcium signal intensity. Scale bar: 20 µm. (**B**) Normalized calcium signal intensity of MDA-MB-231 cells on 2D following the application of prescribed hydrostatic pressure differentials at t=0 min. Data are normalized to those of the respective unstimulated controls and represent mean±SEM (n>30 cells from 3 independent experiments). (**C**) Representative graph of the normalized calcium intensity of MDA-MB-231 cells over time upon consecutive increases or decreases of hydrostatic pressure (average of 10 cells): (**i**) application of +3 Pa by addition of a prescribed amount of media. (**ii**) a second application of +3 Pa. (**iii**) -10 Pa by aspirating media. (**iv**) +10 Pa by addition of media. Data are normalized to the signal of unstimulated cells, and represent mean±SEM. (**D**) Normalized calcium signal intensity of MDA-MB-231 cells on 2D following the application of 3 Pa hydrostatic pressure differential at t=0 min in response to vehicle control or Latrunculin A and FTY720 treatments (n>30 cells from 3 independent experiments). Data represent mean±SEM. (**E**) Representative Western blot illustrating the efficiency of TRPM7 knockout in MDA-MB-231 cells. β-actin is used as a loading control. (**F**) and (**G**) Mean±SEM of intracellular Ca^{2+} signals (Fura-2 ratio) obtained in HEK293 cells transfected with GFP (n=28), TRPM7 (n=50), TRPV4 (n=92), Piezo1 (n=84), Piezo2 (n=72) or TRPM7 pre-treated with blebbistatin (n=28). Cells were stimulated with a hydrostatic pressure differential of 30 Pa. (**H**) Mean current densities measured at +100 mV and – 100 mV in HEK293 cells overexpressing mouse TRPM7 in the presence of blebbistatin (n=4). (**I**) Representative images depicting the algorithm for quantification of cortical myosin from MIIA-GFP-labeled MDA-MB-231 cells (cell in Fig. 3G). (**i**) Original MIIA-GFP image. (**ii**) Image after binary thresholding. (**iii**) Image depicting the contour length of cortical MIIA. (**iv**) Image depicting the filtered MIIA-GFP signal. Representative graphs of the cortical width and integrated signal intensity of myosin (**J**) and actin (**L**) from MIIA-GFP- and LifeAct-Ruby2-labeled MDA-MB-231 cells, respectively, as a function of time (cells in Fig. 3G and fig. S3K, respectively). A 3 Pa hydrostatic pressure differential was applied at t=0 min. (**K**) Representative image sequence depicting the LifeAct-Ruby2 signal of an MDA-MB-231 cell before and after the application of a 3 Pa hydrostatic pressure differential. Hydrostatic pressure is applied right after (**ii**). Scale bar: 10 µm. (**v**) Kymograph of the line scan showed in (**i-iv**). Yellow arrow indicates the first frame after the application of a hydrostatic pressure differential. Following image segmentation, each pixel's intensity value was assigned a color according to ImageJ's fire heat map for visualization purposes.

Fig. S4

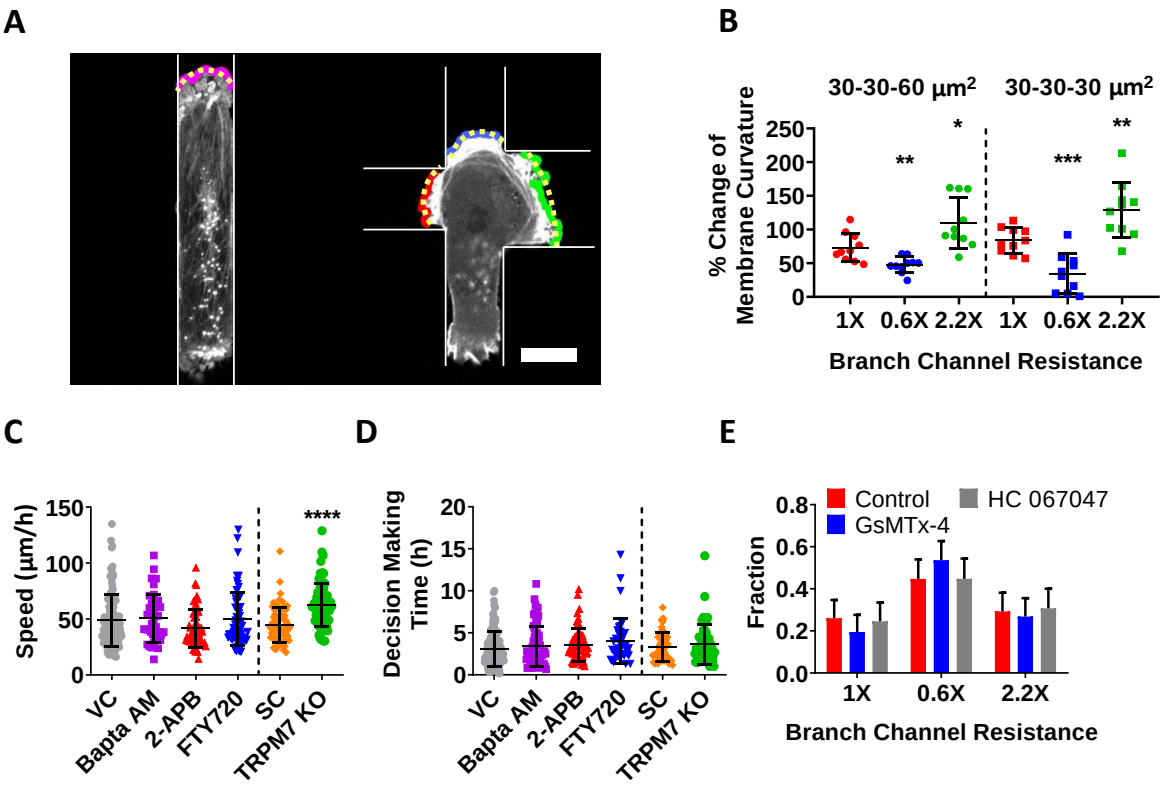

Fig. S4. High hydraulic resistance results in larger changes of membrane curvature. (**A**) Representative images indicating the edges of the membrane protrusions of a LifeAct-GFP-labeled MDA-MB-231 cell at the feeder channel (left image) and when it first occludes the intersection (right image). Membrane protrusions are colored purple (at the feeder channel), red (protrusion in 1X), blue (protrusion in 0.6X), green (protrusion in 2.2X). Dotted line represents the fitted second order polynomial indicating the membrane curvature. White solid lines indicate the edges of the microchannels. Scale bar: 10 µm. Image segmentation was applied to both images. (**B**) Percent change of membrane curvature of each protrusion of MDA-MB-231 cells in branches of different hydraulic resistances as compared to the curvature in the feeder channel using two different microfluidic designs (n=10 cells from >3 independent experiments for each design). The cross-sectional areas of left, straight and right branches of the two designs are denoted above the graph. Data represent the mean±SD. One-way ANOVA with post-hoc Tukey was performed. *p<0.05, **p<0.01, ***p<0.001 relative to cells in 1X channel. (**C**) Migration speeds of MDA-MB-231 cells in the feeder channel prior to reaching the intersection in response to different pharmacological (BaptaAM, 2-APB, FTY720) or molecular (TRPM7-KO) interventions (n>40 cells from 3 independent experiments for each condition). Data represent the mean±SD. Two-tailed unpaired t test performed, ****p<0.0001 relative to scramble control. (**D**) Decision-making time of MDA-MB-231 cells in response to different pharmacological (BaptaAM, 2-APB, FTY720) or molecular (TRPM7-KO) interventions (n>40 cells from 3 independent experiments). Data represent the mean±SD. (**E**) Distribution pattern of MDA-MB-231 cells in branch channels of different hydraulic resistances in response to different pharmacological

inhibitors (HC 067047 and GsMTx-4) (n>100 cells from 3 independent experiments). Data represent the mean with 95% confidence interval.

Fig. S5

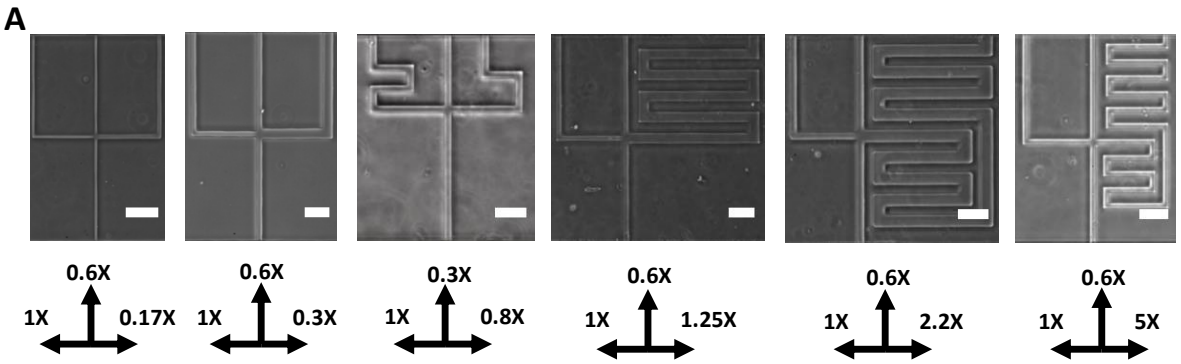
A
0.6X
1X
0.17X
0.6X
1X
0.3X
0.3X
1X
0.8X
0.6X
1X
1.25X
0.6X
1X
2.2X
0.6X
1X
5X

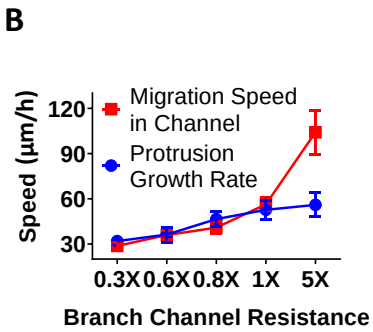
B
Speed (μm/h)
120
90
60
30
Migration Speed in Channel
Protrusion Growth Rate
0.3X 0.6X 0.8X 1X 5X
Branch Channel Resistance

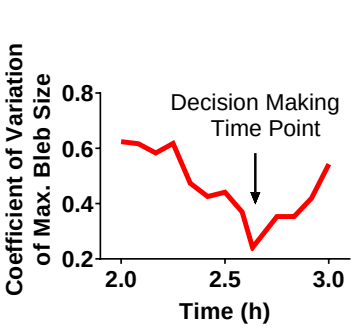
C
Coefficient of Variation of Max. Bleb Size
0.8
0.6
0.4
0.2
Decision Making Time Point
2.0
2.5
3.0
Time (h)

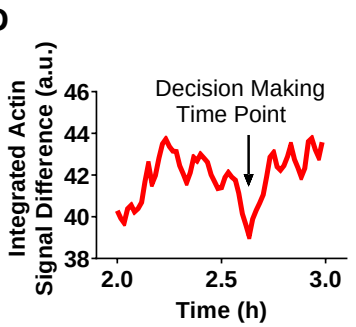
D
Integrated Actin Signal Difference (a.u.)
46
44
42
40
38
Decision Making Time Point
2.0
2.5
3.0
Time (h)

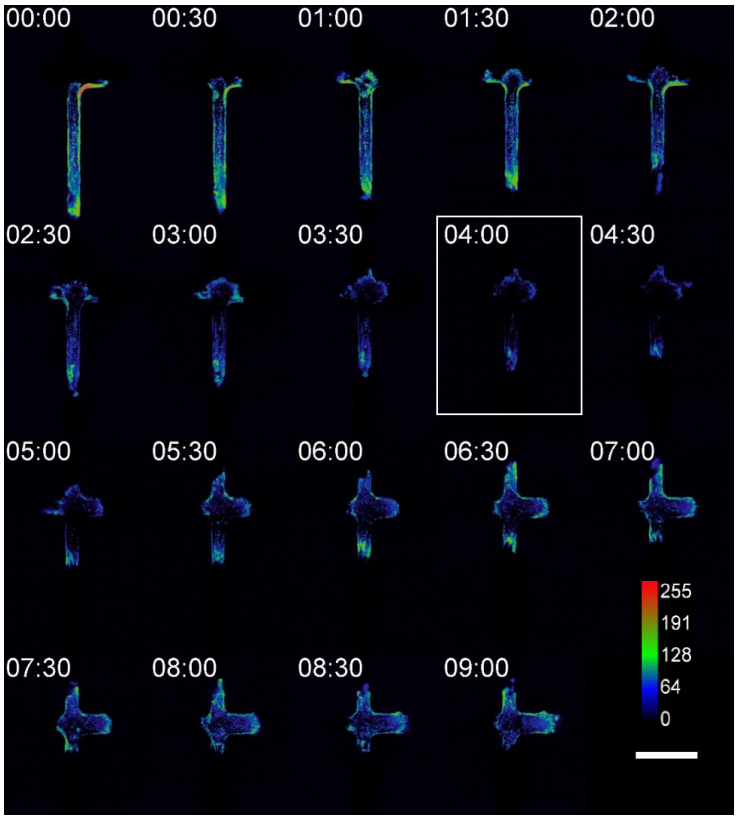
E
00:00
00:30
01:00
01:30
02:00
02:30
03:00
03:30
04:00
04:30
05:00
05:30
06:00
06:30
07:00
07:30
08:00
08:30
09:00
255
191
128
64
0

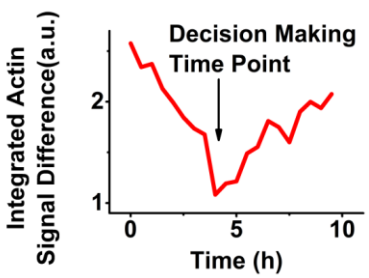
F
Integrated Actin Signal Difference(a.u.)
2
1
Decision Making Time Point
0
5
10
Time (h)

Fig. S5

G

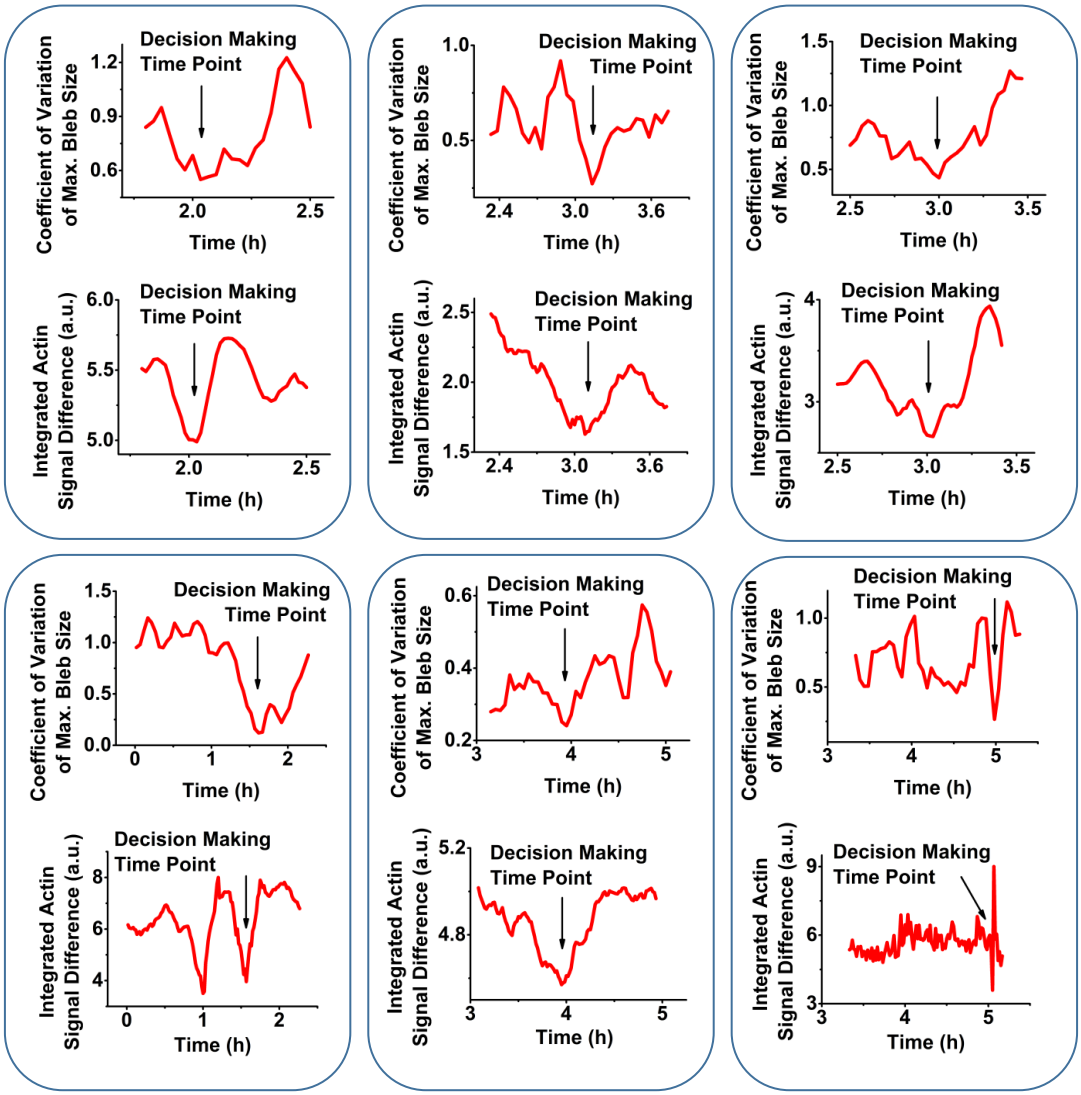
Coefficient of Variation of Max. Bleb Size
Integrated Actin Signal Difference (a.u.)
Decision Making Time Point
Time (h)

Fig. S5

H

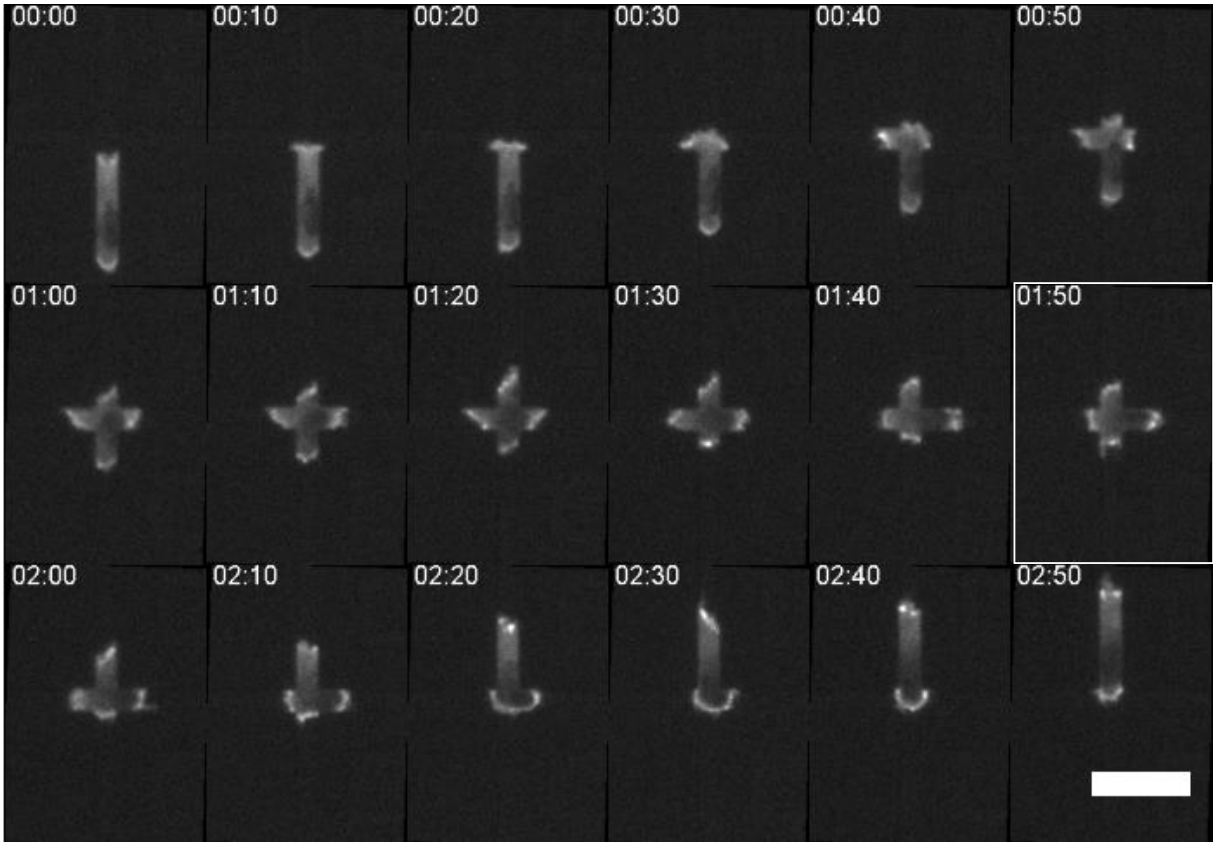

Fig. S5. Variations in bleb size and cortical actin intensity reach a minimum at the decision-making time point, suggesting a physical balance between internal and external cell forces. (**A**) Phase contrast images of different Ψ-like trifurcating microfluidic devices used in Fig. 5D. Arrows below each design indicate the direction of branch channels and their respective relative hydraulic resistance. Scale bar: 50 μm. (**B**) Speed of protrusion growth during stage 2 (see Fig. 1E) and speed of migration at stage 3 (see Fig. 1E) of MDA-MB-231 cells (n>10 cells for each data point from 3 independent experiments). Data represent the mean±SD. (**C**) Coefficient of variation of maximum bleb size among the three protrusions inside the branch channels of the trifurcating microfluidic device shown in Fig. 1A. Arrow indicates the decision-making time point. (**D**) Difference in the integrated actin signal intensity of a cell between consecutive time frames. Arrow indicates the decision-making time point. (**E**) Representative image sequence of the difference of actin signal intensity between consecutive frames (as calculated by frame to frame subtraction) of a LifeAct-GFP-labeled MDA-MB-231 cell during the decision-making process. The decision-making time point is at t=4 h. Black color indicates no change in actin intensity. Scale bar: 50 μm. (**F**) Integrated actin signal intensity variation of the representative cell in **fig. S5E**. Arrow indicates the decision-making time point. (**G**) Six examples of the coefficient of variation of maximum bleb size among the three cell protrusions inside branch channels (top panels) and the integrated actin signal difference between consecutive images (bottom panels) as a function of time. Arrows indicate the

decision-making time points. (**H**) Representative image sequence of MIIA-GFP localization in a MDA-MB-231 cell inside a Ψ-like trifurcating microfluidic device shown in Fig. 1A during the decision-making process. The white box represents the decision-making time point. After this point, myosin IIA redistributes from the recessive protrusions to the cell trailing edge. The contrast of the fluorescent signal has been increased in all images uniformly for visualization purposes.

Table S1. Dimensions of the different trifurcated designs.

Relative Hydraulic Resistance	Direction of Channel at the Intersection	Width (μm)	Height (μm)	Length (μm)
1X – 0.6X – 0.17X	L	3	10	320
	S	3	10	200
	R	6	10	320
1X – 0.6X – 0.3X	L	10	3	320
	S	10	3	200
	R	20	3	320
1X – 0.3X – 0.8X	L	10	3	320
	S	10	3	100
	R	10	3	260
1X – 0.6X – 1.25X	L	10	3	320
	S	10	3	200
	R	20	3	1280
1X – 0.6X – 2.2X	L	10	3	320
	S	10	3	200
	R	20	3	2240
1X – 0.6X – 5X	L	10	3	320
	S	10	3	200
	R	10	3	1600

The relative hydraulic resistance of each branch channel is given in the following order: L-S-R (corresponding to left, straight and right branch channel, respectively).

Table S2. Comparison between the experimental and theoretical probabilities of cells entering branches in two different devices. Determination of the expression of M_i ($M_i = I_i A_i$) and value of β (β=1.67) by fitting the theoretical to the experimental probability of cells entering the left, straight or right branch channels at the trifurcations, using two different microfluidic designs.

Design and Relative Hydraulic Resistances in Microchannel Branches		**Experimental Probability**	**Fitted Probability (p_i)**	**Difference**
Design1 (1X – 0.6X – 0.17X)	Left (1X)	0.21	0.22	0.01
	Straight (0.6X)	0.27	0.29	0.02
	Right (0.17X)	0.51	0.48	0.03
Design 2 (1X – 0.6X – 0.3X)	Left (1X)	0.21	0.21	0
	Straight (0.6X)	0.28	0.31	0.03
	Right (0.3X)	0.50	0.47	0.03

Table S3. Comparison between the experimental and theoretical probabilities of cells entering branches in multiple devices. Using the fitted parameters of M_i and β reported in Table S2 as inputs in three separate microfluidic designs, the predicted probability distributions successfully matched experimental data.

Design and Relative Hydraulic Resistances in Microchannel Branches		**Predicted Probability**	**Experimental Probability**	**Difference**
Design 3 (1X – 0.3X – 0.8X)	Left (1X)	0.22	0.24	0.02
	Straight (0.3X)	0.47	0.47	0
	Right (0.8X)	0.31	0.29	0.02
Design 4 (1X – 0.6X – 1.25X)	Left (1X)	0.29	0.27	0.02
	Straight (0.6X)	0.41	0.41	0
	Right (1.25X)	0.29	0.32	0.03
Design 5 (1X – 0.6X – 2.2X)	Left (1X)	0.25	0.24	0.01
	Straight (0.6X)	0.46	0.46	0
	Right (2.2X)	0.29	0.30	0.01